

Visual Demonstration of Three-Scale Sea-Surface Roughness Under Light Wind Conditions

Edward J. Walsh, *Senior Member, IEEE*, Michael L. Banner, James H. Churnside, Joseph A. Shaw, *Senior Member, IEEE*, Douglas C. Vandemark, *Member, IEEE*, C. Wayne Wright, Jorgen B. Jensen, and Sunhee Lee

Abstract—During the Southern Ocean Waves Experiment (SOWEX) an aircraft carried a down-looking video camera to help document the sea surface. Reflected images of the aircraft were intermittently observed in the video recorded at 15–30-m height under light and variable wind conditions. A numerical simulation was developed to relate image contrast to the gravity-capillary wave contribution to sea-surface mean square slope (mss). “Carnival fun-house” mirror-type distortions of the image in the absence of the gravity-capillary waves relate to intermediate-scale wave persistence when wind forcing stops. Video image estimates of mss correlated better with 36-GHz scanning radar altimeter estimates than with the wind speed measured at 30-m height. When the gravity-capillary waves disappeared in the absence of wind forcing, about one-third of the 0.0015 residual mss was contributed by the dominant waves, and about two-thirds was contributed by the 1–10-m wavelength region. Near the shores of a lake in Alaska, reflected aircraft images were also observed, indicating that the gravity-capillary wave contribution to mss was only about 0.000 001, even though the wind speed at the 160-m aircraft height was 10 m/s.

Index Terms—Light wind, mean square slope (MSS), microwave, optical, sea surface.

I. INTRODUCTION

AREAS of unusually low sea-surface mean square slope (mss) adversely affect almost 6% of the over ocean data of the TOPEX satellite radar altimeter [1]. The unusually high radar cross section of these areas at nadir and its rapid decrease with small increases in incidence angle distort the altimeter return waveform, causing errors in the range measurements. Regions of low wind speed and mss also exhibit an intermittency

Manuscript received August 18, 2004; revised November 11, 2004. This work was supported in part by the National Aeronautics and Space Administration Physical Oceanography Program, in part by the Australian Research Council, in part by the National Science Foundation, in part by the Commonwealth Scientific and Industrial Research Organization (CSIRO) Marine Laboratory, and in part by the CSIRO Office of Space Science and Applications.

E. J. Walsh, D. C. Vandemark, and C. W. Wright are with the NASA Goddard Space Flight Center, Wallops Flight Facility, Wallops Island, VA 23337 USA (e-mail: Edward.Walsh@nasa.gov).

M. L. Banner is with the Department of Mathematics, The University of New South Wales, Sydney 2052, Australia.

J. H. Churnside is with the NOAA Environmental Technology Laboratory, Boulder, CO 80305-3328 USA.

J. A. Shaw was with the NOAA Environmental Technology Laboratory, Boulder, CO 80305-3328 USA. He is now with the Department of Electrical and Computer Engineering, Montana State University, Bozeman, MT 59717 USA.

J. B. Jensen was with CSIRO Atmospheric Research, Aspendale, Victoria 3195, Australia. He is now with the National Center for Atmospheric Research, Research Aircraft Facility, Broomfield, CO 80021 USA.

S. Lee is with CSIRO Marine and Atmospheric Research, Aspendale, Victoria 3195, Australia.

Digital Object Identifier 10.1109/TGRS.2005.851633

that adversely affects the measurement of global wind speeds by spaceborne scatterometers [2], [3]. This paper does not investigate either of those phenomena, but describes a new technique accidentally discovered during the Southern Ocean Waves Experiment (SOWEX) [4], [5] which might provide low cost, high spatial and time resolution measurements of sea-surface mss in the gravity-capillary region under conditions responsible for the “ σ^0 blooms” of the nadir-looking altimeters and the intermittency affecting the off-nadir-looking scatterometers.

SOWEX was conducted in June 1992 out of Hobart, Tasmania. The National Aeronautics and Space Administration (NASA) Scanning Radar Altimeter (SRA) [6]–[8] was shipped to Australia and installed on a Commonwealth Scientific and Industrial Research Organization (CSIRO) Fokker F-27 research aircraft instrumented to make comprehensive measurements of air–sea interaction fluxes. It also carried a down-looking video camera to help document the sea surface. During a flight under light and variable wind conditions on June 16, reflected images of the aircraft were intermittently observed on the video monitor when the aircraft was at 15–30-m height, which prompted this analysis.

The SRA sweeps a radar beam of 1° (two-way) half-power width across the aircraft ground track over a swath equal to 0.8 of the aircraft height, simultaneously measuring the backscattered power at its 36 GHz (8.3 mm) operating frequency and the range to the sea surface at 64 cross-track positions at measurement angles fixed within $\pm 22^\circ$ with respect to the normal to the aircraft wings.

The NASA SRA slant ranges are multiplied by the cosine of the off-nadir incidence angles (including the effect of aircraft roll attitude) to determine the vertical distances from the aircraft to the sea surface. These distances are subtracted from the aircraft height to produce a sea-surface elevation map, which is displayed on a monitor in the aircraft to enable real-time assessment of data quality and wave properties. The falloff of backscattered power with incidence angle can be used to determine the sea-surface mean square slope (mss), filtered by the 8.3-mm transmitted wavelength. The light wind during the flight over the Southern Ocean on June 16, 1992 provided an opportunity to relate the mss to the visual appearance of the reflection of the aircraft in the sea-surface imagery captured by a down-looking video camera. This helps put a “face” on the state of the sea surface and its variability under light wind conditions.

Fig. 1 shows the aircraft flight track for a 2.3-h interval on June 16. After leaving the coast of Tasmania at 1.4-km altitude, the aircraft descended to 440 m (**a**). The three small circles

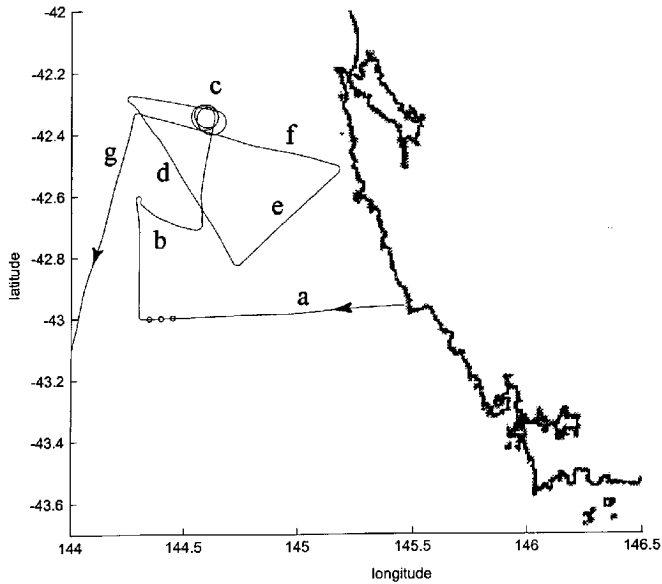


Fig. 1. Flight track of Fokker F-27 aircraft off the western coast of Tasmania, Australia, on June 16, 1992.

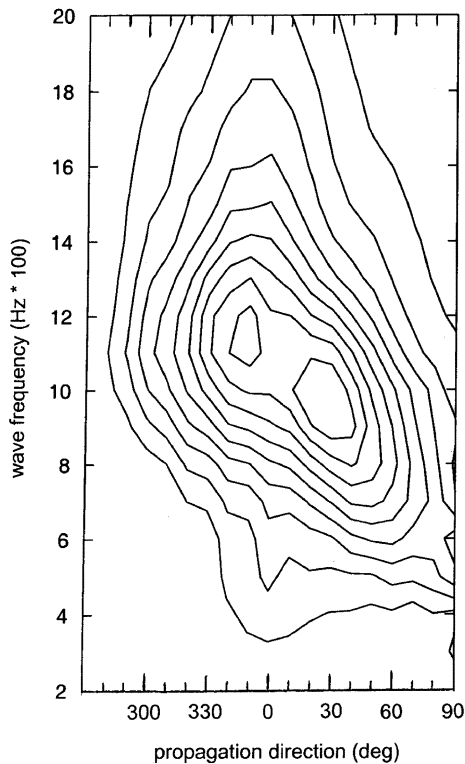


Fig. 2. Average of three directional wave spectra computed from contiguous sea-surface topography spans measured by the SRA, whose centers are indicated by the three circles on flight segment *a* in Fig. 1. The linear contours span from 0.1–0.9 of the spectral peak density.

indicate the centers of three contiguous SRA data spans used to generate directional wave spectra. The average of the three spectra, additionally smoothed over 0.03 Hz and 30°, is shown in Fig. 2. The significant wave height (H_S) was 2.1 m. The dominant waves had 120–160-m wavelength and propagated toward 350° to 30°. After the aircraft turned north, it dropped to 15-m altitude and did a sounding to 1.5 km (*b*), followed by a series of circles at 240-m altitude to measure the azimuthal dependence

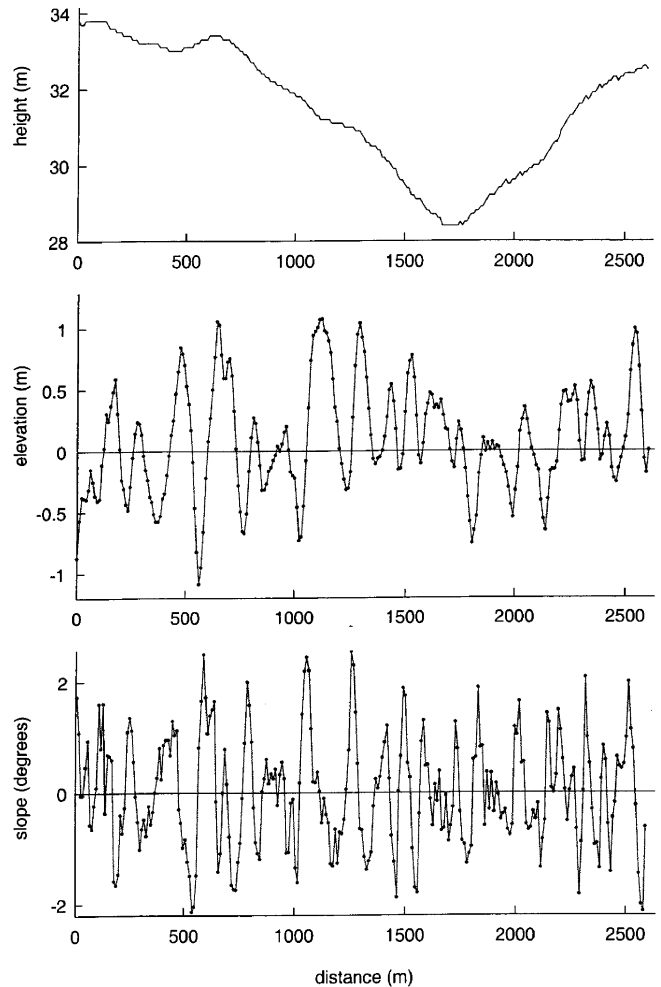


Fig. 3. Aircraft (top panel) height and (middle panel) along-track sea-surface elevation profile and (bottom panel) slope measured by the SRA on flight segment *g* in Fig. 1.

of the radar backscatter cross section (*c*). A triangle (*d*, *e*, *f*) was flown at 10–15-m height to measure fluxes.

The focus of this paper is the track flown at about 30-m height toward 195° (*g*), approximately into the swell propagating out of the Southern Ocean. The aircraft ground speed was 76 m/s, and 15 m/s was used as a representative phase speed for the swell propagating toward the aircraft, producing an approximate relative speed over the waves of 91 m/s. The NASA SRA 10-Hz cross-track scan rate resulted in an along-track wave-relative scan line spacing of 9.1 m. The top panel of Fig. 3 shows the aircraft height variation over a wave-relative 2.5-km interval along track (*g*) using 9.1 m per scan line.

The middle panel shows the surface elevation profile measured by the SRA. Each point in the elevation profile was obtained by using a random consensus filter [9] on the 18 elevations nearest nadir in each 64-point cross-track scan. At 31-m height, the swath width was 25 m and the cross-track extent of the 18 points nearest nadir was only 7 m, less than the along-track separation of the scan lines. The random consensus filter concept is very simple. First, a reasonable span for the local observations (each group of 18 cross-track points nearest nadir) is established. One meter was considered the maximum vertical extent within which valid elevation measurements could

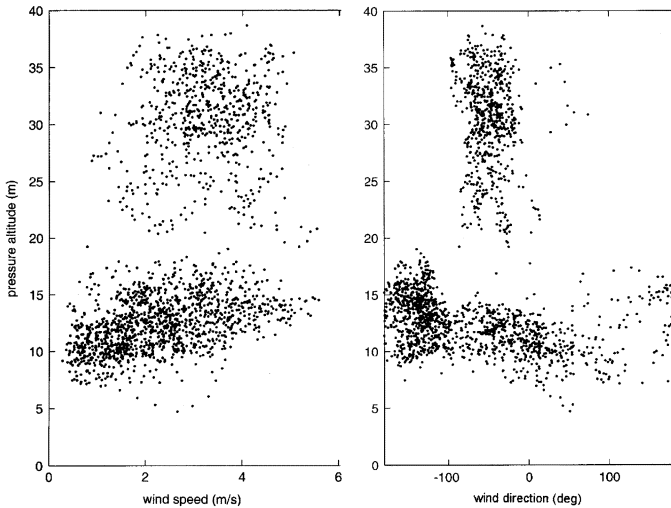


Fig. 4. Variation of wind speed and direction with height for the portions of flight segments *d*, *f*, and *g* (Fig. 1) within 20 km of 42.332° S, 144.3° E. These data were acquired within a 55-min time interval.

exist considering (a) random variations in the SRA range measurements caused by fluctuations in the scattered signal, and (b) cross-track changes in sea-surface elevation. Second, a window of that extent is shifted vertically until it contains the maximum number of points out of each set of 18. Third, values outside the window are discarded as outliers and values within the window are averaged. The consensus-filtered values of SRA elevation were further smoothed by an along-track three-point filter before being plotted in the middle panel of Fig. 3.

The bottom panel shows the along-track slope obtained by differencing the elevation values in the middle panel. The maximum slopes were about $\pm 2^\circ$ and occurred on the leading and trailing faces of the swell, with the leading faces (positive slopes) generally being steeper.

Fig. 4 shows the variation of wind speed and direction with height measured by the aircraft for the portions of flight segments *d*, *f*, and *g* (Fig. 1) which were within 20 km of 42.332° S, 144.3° E, approximately where flight segment *d* crossed the corner formed by *f* and *g*. The data in Fig. 4, acquired within a 55-min time interval, indicate that the wind at 10-m height was statistically lower in speed and much more variable in direction than at 30-m height.

In Section II, we will review radar measurement of mss and examine the SRA mss variation along the flight line used for the optical analysis. Section III develops a model for analyzing the optical data. Section IV compares the spatial variations of the radar and optical measurements of mss for an aircraft height of 30 m. Section V examines boundaries for dividing the surface roughness into three scales. Section VI shows an example of the optical technique working from an aircraft at 160-m height. The last section summarizes the paper and discusses the possibility of using the optical technique in a bistatic mode.

II. RADAR MEASUREMENT OF SEA-SURFACE MSS

Under the near-nadir, quasi-specular scattering regime of the SRA geometry, the energy scattered back toward the radar is dependent on the number and effective area of the specular points

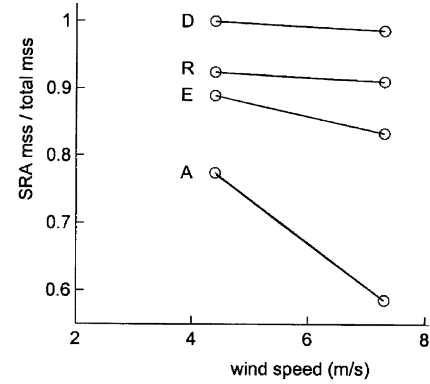


Fig. 5. Computed ratio of the mss measured by the SRA (assuming sea-surface wavelengths shorter than 2.5 cm have been effectively smoothed) to the total mss versus U_{10} wind speed for the spectra of Donelan and Pierson (D) [16], Romeiser *et al.* (R) [18], Elfouhaily *et al.* (E) [19], and Apel (A) [17].

illuminated. For the slope-dependent specular point model [10] of radar sea-surface scattering, which should be applicable out to incidence angles of about 15° , an expression approximated by a geometric optics (GO) form, generalized from Valenzuela's [11], (3.8) for the normalized backscatter radar cross section in an azimuthal look direction Φ would be

$$\sigma_{\text{GO}\Phi}^0 = \rho \sec^4 \theta \text{mss}^{-1} \exp(-\tan^2 \theta / (2 \text{mss}(\Phi))) \quad (1)$$

where ρ is an effective reflectivity, θ is the off-nadir incidence angle, and $\text{mss}(\Phi)$ is the mean square slope of the component of the sea-surface slope vector in the azimuthal direction Φ .

For an isotropic, Gaussian surface [11], [12], $\text{mss}(\Phi)$ is always equal to $\text{mss}/2$, where mss is the total mean square slope of the sea surface, and (1) reduces to the expression for the normalized radar cross section generally used in pulse-limited altimetry

$$\sigma_{\text{GOG}}^0 = \rho \sec^4 \theta \text{mss}^{-1} \exp(-\tan^2 \theta / \text{mss}). \quad (2)$$

The mss in (2) affects both the magnitude of the radar cross section at nadir and its rate of falloff with increasing incidence angle. The SRA determines mss from the falloff of the radar cross section with incidence angle using only relative power measurements. If (2) is normalized by its peak for each value of mss, it becomes

$$\sigma_{\text{rel}}^0 = \sec^4 \theta \exp(-\tan^2 \theta / \text{mss}). \quad (3)$$

Taking the natural logarithm of (3) results in

$$\ln(\sigma_{\text{rel}}^0) = \ln(\sec^4 \theta) - \text{mss}^{-1} \tan^2 \theta. \quad (4)$$

Equation (4) can be rewritten in the form

$$\ln(\sigma_{\text{rel}}^0) = -(\text{mss}^{-1} - A) \tan^2 \theta \quad (5)$$

where $A = \ln(\sec^4 \theta) / \tan^2 \theta$. For small angles, A is approximately constant. Its value is 2 at $\theta = 0$, decreasing in a quadratic fashion to 1.93 as θ increases to 15° . For the values of mss considered in this paper (about 0.015 or less), neglecting the A term in (5) causes less than a 3% error in the mss determination

$$\ln(\sigma_{\text{rel}}^0) \approx -\text{mss}^{-1} \tan^2 \theta, \quad \text{mss} < 0.015. \quad (6)$$

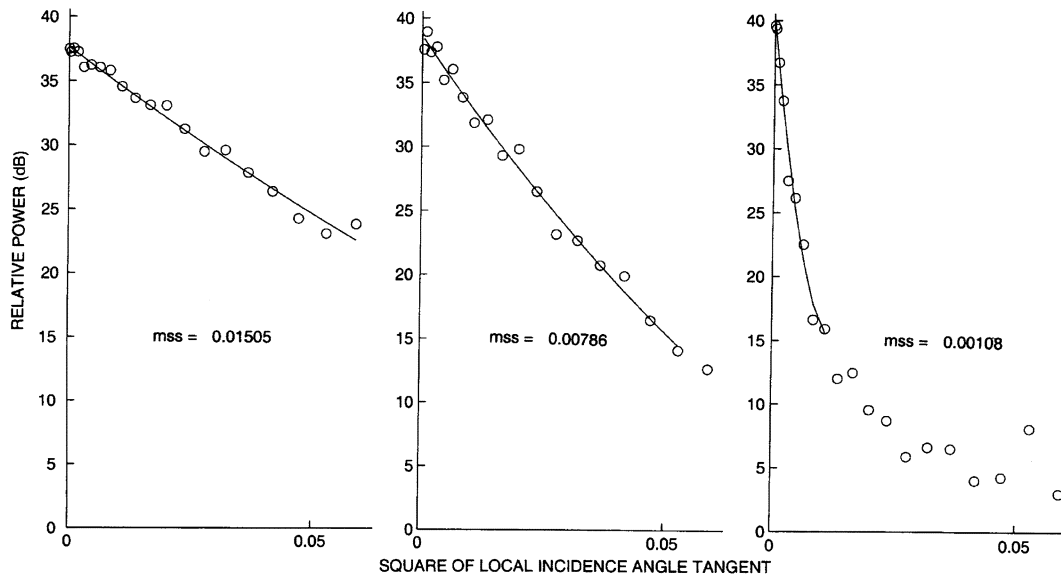


Fig. 6. Backscattered power at 36 GHz as a function of incidence angle measured by the SRA at three different positions along flight segment g in Fig. 1.

For low values of mss (light wind conditions), mss is just the reciprocal of the slope of the decrease of the log of the backscattered power plotted against the tangent of the incidence angle squared.

To what extent does a radar operating at 36 GHz (8.3-mm wavelength) effectively smooth over the sea surface, eliminating a portion of the mss ? The largest contribution to mss is generally provided by the gravity-capillary wavenumber spectrum. Measurements in this domain have frequently been aimed at determining a fully developed short wave spectrum which could then be used to relate the outputs of remote sensors to wind speed. Determinations have been made using scanning laser slope sensors [13]–[15] and inferred by adjusting spectral parameters to provide the best fit to sea-surface radar backscatter data [16]–[18] or optical data [19]. Trokhimovski [20] retrieved wave parameters from a set of radiometric measurements collected from a blimp at several incidence angles, polarizations, and wavenumbers.

Brown [21] reviewed the theoretical status of quasi-specular scattering from the air–sea interface in 1990. Millet and Warnick [22] recently discussed many of the developments of the last 15 years, pointing out that the determination of validity criteria for rough surface scattering models continues to be an active area of research.

In two-scale models the wave spectrum is divided into large and small scales with the large-scale corresponding to the Kirchhoff solution for the specular reflections and the small scale corresponding to the Bragg scattering solution, which is generally neglected near nadir. Jackson *et al.* [23] tabulated the choices of seven investigators as to the wavelength separating the large and small-scale regimes. They ranged from 1.5 to 40 times the radar wavelength. Using the Elfouhaily *et al.* [19] spectrum, Voronovich and Zavorotny [24] compared the results of a small-slope approximation numerical computation with the results for the two-scale computation for separation boundaries of 3, 10, and 40 times the 2.14 cm (Ku-band) radar wavelength.

The three-wavelength boundary produced the best agreement and that smoothing criterion will be adopted here.

For wind speeds of 4.4 and 7.3 m/s, Trokhimovski [20] computed the expected value of mss as a function of cutoff frequency for four spectra [16]–[19]. Fig. 5 shows the ratio of the mss expected for the SRA 0.83-cm electromagnetic wavelength (2.5-cm sea-surface cutoff wavelength) to the total mss . All the spectra indicate that the truncated to total mss ratio increases as wind speed is reduced. The Donelan and Pierson [16] and Romeiser *et al.* [18] ratios are already above 90% for an 8-m/s wind speed. That would also be the case for a spectrum recently proposed by Plant [25] as a composite based on three other spectra [26]–[28]. Apel's [17] spectrum predicts the lowest ratio in Fig. 5 because it has significantly larger high wavenumber content than the other spectra. Since measurements [15], [29] indicate that the spectral density of wavelengths shorter than 2.5 cm decreases rapidly with speed for low wind conditions, it is not unreasonable to assume that the SRA mss would typically be nearly equal to the total mss for U_{10} in the 0–4-m/s range.

Fig. 6 plots the falloff of backscattered power (in decibels) measured by the SRA on June 16, 1992 at three positions along track g (Fig. 1) versus the square of the incident angle tangent. Each plot shows the data from 20 cross-track scan lines (2 s) with the backscattered power from the left and right sides of the aircraft averaged to increase the degrees of freedom of the fluctuating signal. The three mss values (0.015, 0.008, and 0.001) demonstrate the dramatic variation of the power falloff with changes in mss .

When considering non-Gaussian statistics, the typical assumption is that the composite surface small-scale roughness caused by the gravity-capillary waves is locally Gaussian. But the spatial variation of that roughness due to wind variation or modulation by the large-scale tilts of the gravity wave field can lead to non-Gaussian properties over a larger area [30].

The non-Gaussian characteristic is that larger slopes are more probable than for the Gaussian case and a better fit to the data

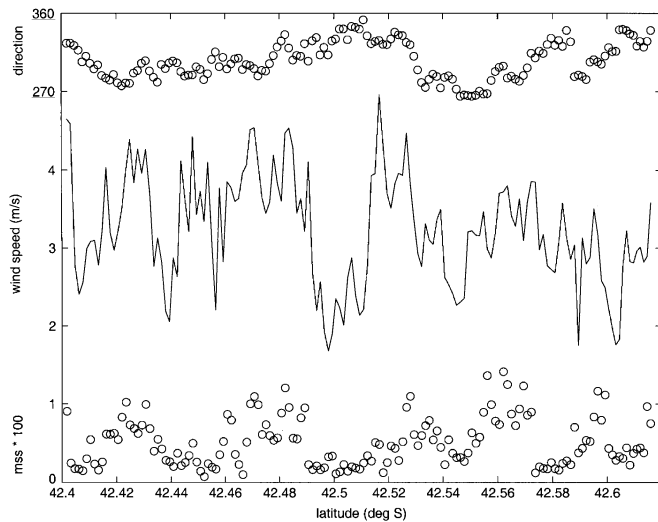


Fig. 7. Wind speed and direction at the aircraft altitude and mss measured by the SRA along flight segment *g* in Fig. 1.

results using the quadratic curves shown in Fig. 6 instead of the straight lines suggested by (6). Using linear fits results in an mss determination that increases as the incidence angle span increases [31]. The quadratic curves of Fig. 6 were fit to the relative power values that were within 25 dB of the peak.

Fig. 7 shows for a 24-km interval along track *g* (Fig. 1) the variation of the sea-surface mss determined by the SRA as well as the wind speed and direction at the 30-m aircraft height. The wind speed fluctuated between about 1.5 and 5 m/s, and its direction varied between about west and north. The air temperature measured when the aircraft was at 15-m height was 9.1 °C. A Barnes radiometer indicated the water temperature was 11.7 °C, 2.6 °C warmer than the air temperature.

The mss tends to be lower when the wind speed is lower, but despite the unstable atmospheric conditions, the wind speed at the surface would not be expected to perfectly correlate with the wind at 30-m height. The aircraft intercom was recorded and the pilots can be heard discussing the small-scale waves they observed on the surface along track *g*. They indicated that the surface wind varied between coming directly from the right side of the aircraft (285°) to being 30° or 40° to the right of the aircraft nose (225° to 235°). The pilots also described the convergence zones between these areas of different wind directions as having the appearance of oily streaks, no doubt caused by an accumulation of surfactants. Surfactants can cause a significant reduction in mss and probably account for the abrupt drop in mss at about 42.57°S in Fig. 7.

III. VISUALIZING SMALL- AND INTERMEDIATE-SCALE SURFACE WAVE EFFECTS

Fig. 8 shows the CSIRO Fokker F-27 aircraft drawn to scale at a height of 33 m above the sea surface. For convenience of the illustration, the down-looking video camera is represented at the center of the aircraft. The Fokker F-27 is almost 24 m in length, and its image on a mirror surface would be slightly less than 12 m long and subtend an angle of $\pm 10^\circ$ in the video camera field of view.

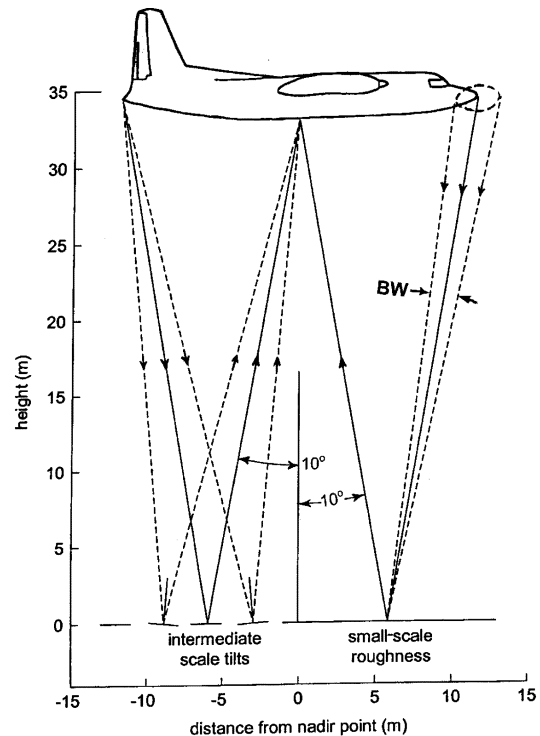


Fig. 8. Fokker F-27 aircraft drawn to scale at 33 m above sea surface on flight segment *g* in Fig. 1.

Although each small nonhorizontal area on the sea surface affects the rays incident on it in the same fashion, it is convenient to consider the composite effect in terms of three wave scales. If the sea had a mirror surface with only a large-scale wave propagating on it, the surface below the aircraft would look like a tilting plane and the undistorted aircraft image would just shift back and forth in the field of view of the camera as the aircraft passed over the wave.

An intermediate scale is shown schematically on the left side of Fig. 8 by considering the image distortion due to three surface tilts such as might be associated with the trough of a 12-m gravity wave. The tail of the aircraft would appear at three locations in the image instead of one, or just be extremely broadened, depending on the curvature between the points. This is similar to the “carnival fun-house” mirror effect, where the image is clear but distorted.

The right side of Fig. 8 indicates the effect of small-scale roughness on an otherwise flat surface. Rays downwelling within a cone surrounding the nose of the aircraft could all be scattered into the camera lens from the image point of the aircraft nose on the sea surface because of the range of small-scale surface slopes at that location. The position of the nose would not be displaced or appear multiple times in the image, but the image contrast and crispness would be reduced because many of the rays would be incident from the sky and not the aircraft. We will develop a simulation of this process to relate the small-scale mss to the appearance of the aircraft image in the down-looking video.

The angular deviation of each ray would be twice that of the surface slope affecting it. To first order, the small-scale roughness slope distribution at each point on the surface effectively

produces a Gaussian scattering pattern which spatially smears the image of the aircraft against the bright sky and reduces its contrast.

The incidence angles considered in Fig. 6 for radar backscatter go up to 14° , but the deviations from the specular direction involved in the effective “beamwidth” (BW) of the small-scale scatterers indicated on the right side of Fig. 8 are generally significantly smaller angles. The horizontal displacement D at the height h of the aircraft from the position of the video camera for a ray reflected from a point on a horizontal, smooth sea surface identified by an off-nadir angle θ is

$$D = 2h \tan \theta. \quad (7)$$

If the sea-surface slope at the point of reflection deviates from horizontal by an angle ϕ , the displacement changes by an increment d given by

$$D + d = h \tan \theta + h \tan(\theta - 2\phi). \quad (8)$$

Expanding (8) using small angle approximations leads to

$$d \approx -2h \tan \phi [1 + \tan \theta (\tan \theta - 2 \tan \phi)]. \quad (9)$$

The quantity within the brackets deviates from unity by about 10% or less for the angles considered here. Those variations were neglected for computational efficiency, resulting in

$$d \approx -2h \tan \phi. \quad (10)$$

The surface slopes change the part of the aircraft or sky contributing to a nominal image point in the video. The surface slope distribution normalized to its peak, $\exp(-\tan^2 \phi / \text{mss})$, acts like an antenna pattern which weights the contributions to the aircraft image, diffusing each image point about its specular reflection angle. For small values of mss, the half-power points on this Gaussian distribution would be at $\phi = \pm 0.8326 \text{ mss}^{0.5}$. The deviation from the specular direction for the rays depicted on the right side of Fig. 8 would be twice that of the surface slopes affecting them, indicated by the factor 2 in (10), resulting in an effective scattering half-power “beamwidth” for the small-scale roughness of

$$\text{BW} = 3.33 \text{ mss}^{0.5}. \quad (11)$$

In terms of horizontal displacement d from the nominal location in the plane of the aircraft, the weighting becomes

$$w = \exp(-d^2 / (4h^2 \text{mss})). \quad (12)$$

The maximum displacement in the plane of the aircraft considered in the simulation was

$$d_{\text{max}} = 2h(5 \text{ mss})^{0.5} \quad (13)$$

at which point the weighting factor is less than 1% of its peak value.

A digitized reference image of the aircraft as a black silhouette against a bright sky was developed. Neither the propellers nor the nose boom (of approximately 6-m length) were included in the reference image. The aircraft silhouette was digitized in 0.144-m resolution in the flight direction and 0.071-m resolu-

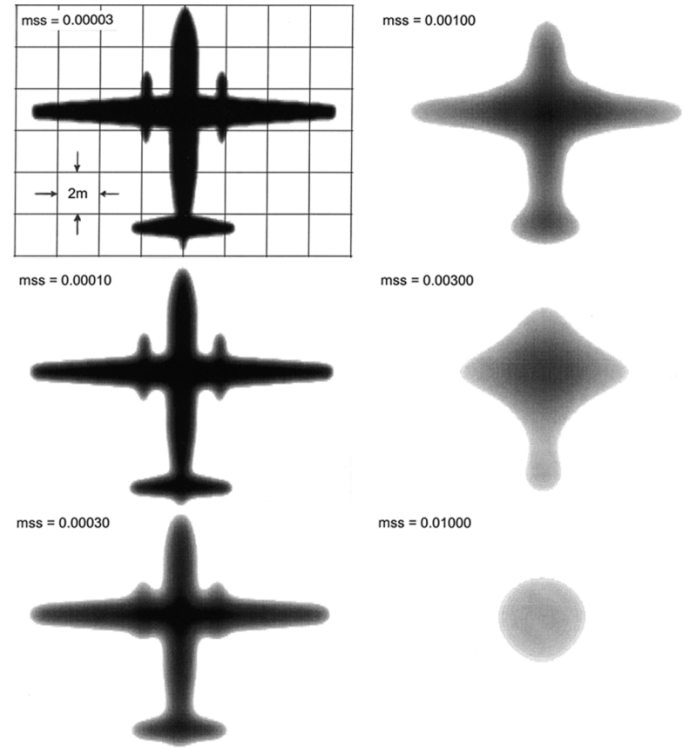


Fig. 9. Numerical simulation of the appearance of the Fokker F-27 aircraft in down-looking video over a flat sea with the indicated values of small-scale roughness.

tion along the wings. Points within the silhouette were assigned a value of 0 (black, aircraft) and points outside were assigned a value of 1 (white, sky). For each value of mss considered in the simulation, a rectangular array of points was generated within $\pm d_{\text{max}}$ using the along-track and cross-track resolutions with weights assigned to them by (12). The weights were then normalized by the sum of all weights in the array.

Each point in the simulated grayscale video images shown in Fig. 9 was generated by multiplying the rectangular array of normalized weights by the pattern of zeros and ones surrounding the nominal position in the plane of the aircraft and summing. Fig. 9 represents the expected image of the aircraft for various values of small-scale mss on an otherwise flat sea surface. The grid in the upper left panel of Fig. 9 indicates the size of the aircraft image on the sea surface, which is half the actual size of the aircraft (Fig. 8).

For $\text{mss} = 0.00003$, $\text{BW} = 1.0^\circ$ and the effective half-power width of the Gaussian scattering pattern at the aircraft height would be only 0.6 m. The aircraft image is nearly the same as the reference image.

For $\text{mss} = 0.0001$ ($\text{BW} = 1.9^\circ$), the half-power scattering pattern width would be 1.1 m at the aircraft, which thickens the image slightly. For $\text{mss} = 0.0003$ ($\text{BW} = 3.3^\circ$), the scattering width would be 1.9 m which causes the engine mounts to almost disappear in the image. At $\text{mss} = 0.001$ ($\text{BW} = 6.0^\circ$), the scattering width would be 3.5 m. Now the engine mounts are gone and the wings have significantly shortened. At $\text{mss} = 0.003$ ($\text{BW} = 10.5^\circ$), the scattering width would be 6.0 m, causing the aircraft image to take on the appearance of a kite.

The Cox and Munk [32]–[34] nominal minimum value of mss is 0.003, and optical measurements of sea-surface rough-

ness [35] indicate the Cox–Munk model requires a modification for stability with higher surface roughness for negative stability (water warmer than air) than for neutral stability for the same wind speed. So one might naively expect that the aircraft appearance would never look more distinct than in the 0.003 mss image of Fig. 9 For $mss = 0.01$ ($BW = 19.1^\circ$), the scattering pattern width at the aircraft height would be 11 m, reducing the aircraft image to a smudge.

The original video on the CSIRO aircraft was recorded at 25 Hz in phase alternation lines (PAL), the 625-line video standard adopted by almost all 50-Hz countries in the world. The PAL format was subsequently translated to the American 525-line National Television System Committee (NTSC) video standard. The frame grabber used to extract digital images for analysis had a maximum rate of about 5.5 frames per second and the images in Fig. 10 are 11 consecutive images from that process, spanning about 2 s, and their average. The video camera recorded all the odd scan lines in the raster first, then all the even scan lines. Since the change in the image over that time interval produced significant smearing, only the odd scan lines are shown in Fig. 10.

There were only scattered clouds along the flight path, but it should be emphasized that the nadir images shown in Fig. 10 were not the shadow of the aircraft because the sun is never overhead at that latitude. The local time span of the 11 images was 15:52:42 to 15:52:43.

The long wavelengths and 2° slopes of the dominant waves (Fig. 3) would produce negligible distortion of the aircraft image. Their main effect would be to shift the image back and forth 10% of the 20° angle subtended by the aircraft in the video frame (Fig. 8). Section I indicated that the approximate relative speed over the dominant waves was $91 \text{ m} \cdot \text{s}^{-1}$. Even at the $76\text{-m} \cdot \text{s}^{-1}$ airspeed, the aircraft moved 13.8 m between images, which was more than the 12-m size of the aircraft image on the sea surface (Fig. 9), assuring total independence.

The aircraft images in Fig. 10 are distorted by the tilts associated with waves of about 1–10-m length. There are times when multiple wings appear (frames 176 and 181) or a single wing with multiple engine housings (frame 178). The thin nose boom is even apparent at times (frames 178 and 179). The high contrast of these images suggests that the small-scale roughness of the sea surface was almost two orders of magnitude lower than the Cox and Munk 0.003 minimum value of mss.

IV. SPATIAL VARIATION OF MSS UNDER LIGHT WIND CONDITIONS

The images of Fig. 10 were unusual in their crispness. The aircraft image appeared and disappeared as the small-scale roughness varied along flight line *g* (Fig. 1). The video images of the aircraft varied in a similar fashion on the lower flight lines of the triangle (*d*, *e*, and *f* in Fig. 1), but the 15-m height was below the operating altitude of the SRA.

The lines connecting the dots in Fig. 11 indicate the optical estimates of mss determined subjectively by comparing the simulations of Fig. 9 with the appearance of the video images along a 24-km segment of flight line *g*. A number from 1 to 6 was assigned at 1-s intervals depending on which of the six images of

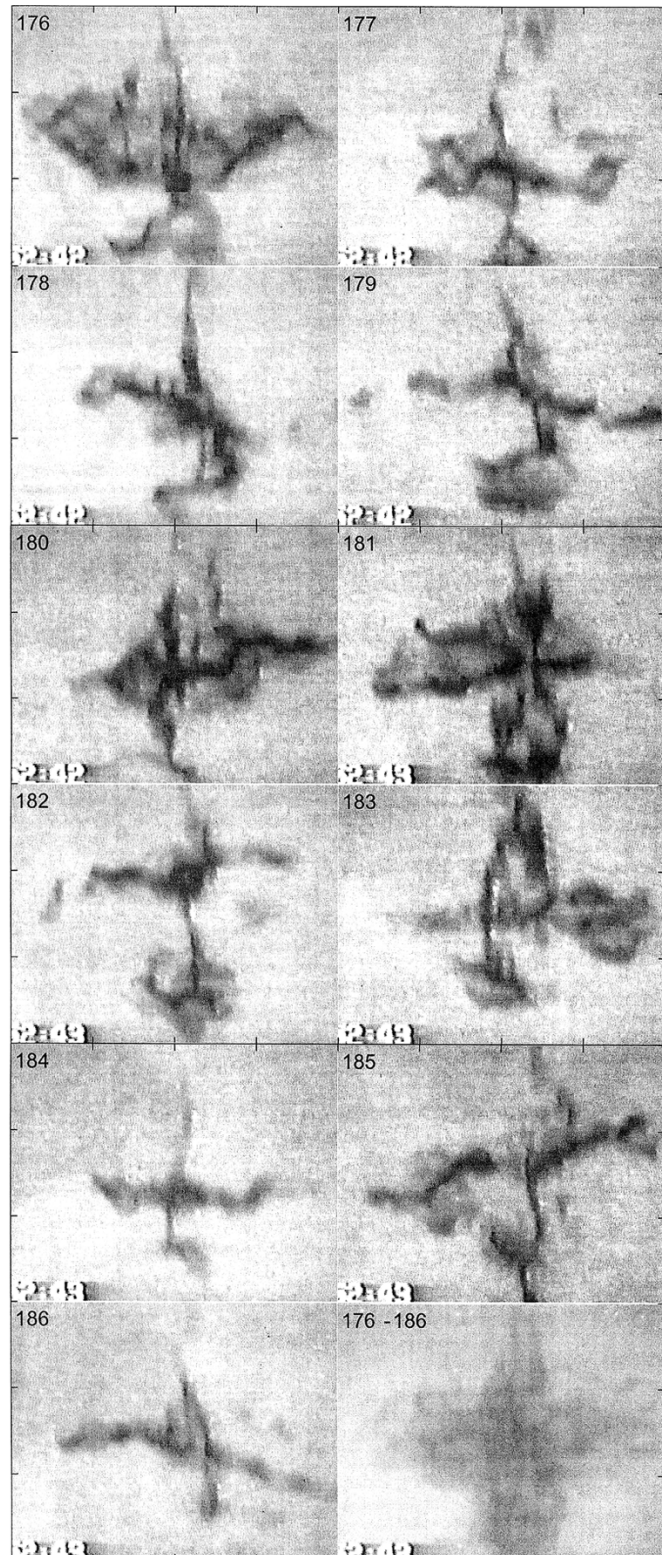


Fig. 10. Eleven frames of the Fokker F-27 aircraft image in the down-looking video and their average, cropped to a width of 18 m on the sea surface. The frame numbers begin with 176 in the upper left-hand image and advance to the right and down, ending with frame 186 in the lower left-hand corner. The aircraft location was in the vicinity of 42.503° S , 144.218° E

Fig. 9 best matched the impression given by the video. Single frame stepping capability for the video was not available so the numbers were written down “on the fly” as the video played in

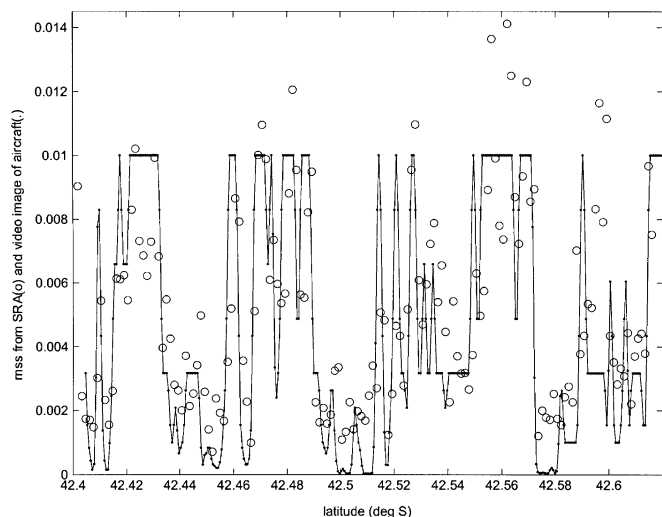


Fig. 11. Estimates of mss from aircraft video image (solid line with dots) and from the SRA microwave backscatter.

real-time. Several passes through the video were made to refine the estimates, but the process was both subjective and imperfect.

Objective techniques could be developed such as computing the standard deviation of the image pixels (smeared out images would have small standard deviations) or Fourier transforming the images to examine spectral content. But that was beyond the scope of this paper and the subjective approach was deemed sufficient for the desired comparison. The subjective mss values were smoothed using a three-point filter whose weights were 0.25, 0.5, and 0.25, to approximate the 2-s average of the 20 scan lines used in the SRA mss determination. The mss values determined from the SRA backscattered power (Fig. 6) are indicated by the circles in Fig. 11, and are the same values shown in Fig. 7.

The quantization of the optical mss estimates before the smoothing was fairly coarse on the linear scale of Fig. 11 with values only at 0.010, 0.003, 0.001, 0.0003, 0.0001, and 0.00003. Despite the crudeness of the “on the fly” video estimates of mss, the agreement is better between the microwave and optical estimations of mss in Fig. 11 than it was between the microwave mss of the SRA and the wind speed at 30-m height shown in Fig. 7. The abrupt drop in both mss determinations at 42.57°S and the joint oscillation in the vicinity of 42.46°S are particularly impressive, although the later suggests there may have been a slight time bias between the SRA clock and the video time tag.

The 11 images of Fig. 10 were in the vicinity of 42.503°S in Fig. 11, where the SRA mss averages about 0.0015. This is reasonable since the optical mss determination was an estimate of the small-scale roughness, and the SRA microwave estimate of mss (Fig. 6) included the longer wavelengths that distorted the optical images without reducing their contrast (Fig. 10).

The simulation in Section III was developed assuming that small-scale roughness caused a Gaussian distribution of surface slopes to exist simultaneously at each position on the sea surface. But the result would be the same if a series of images were taken where there was only one slope at each point on the sea surface (from intermediate and large-scale waves) and then the images were averaged so that the intensity in the average image

would be affected by the collection of surface slopes that sequentially occupied each image point on the sea surface. The average of the 11 images shown in the lower right panel of Fig. 10 would have been considerably smoother if all 50 of the original video frames in this 2-s time interval had been averaged. But even the appearance of the 11-frame average places it somewhere between the 0.001 and 0.003 images in Fig. 9, in good agreement with the SRA estimate.

V. THREE-SCALE BOUNDARIES

Dividing sea-surface roughness into three scales has generally been employed in models aimed at improving the theoretical ocean wave-radar modulation transfer function. The boundaries have varied with the developments but spanned a similar range. In their 1986 study of intensity modulation in synthetic aperture radar (SAR) images of internal waves, Thompson and Gasparovic [36] pointed out that the direct modulation of small-scale roughness by variations in the internal-wave surface current field was insufficient to explain the X-band (~ 3.2 cm) observations. They hypothesized additional small-scale roughness variation produced by the strong perturbation of intermediate-scale wind waves in the 0.628–6.28-m range by the internal wave current field. The intermediate-scale waves would then lose energy to the small-scale waves through nonlinear interactions and breaking.

In their Bragg scattering model development, Romeiser *et al.* [37] defined the intermediate scale as wavelengths large compared to the Bragg wavelength but smaller than the radar resolution cell. Plant [25], in his recent general backscatter model development to cover incidence angles from nadir out to 80°, used an intermediate scale whose boundaries varied with incidence angle and wind speed but which typically spanned from five times the Bragg wavelength to about 10 m (W. J. Plant, personal communication, 2004).

The present study is different from the ones just cited in that they postulated interaction among the wave scales in the steady state to explain the response of remote sensors. Under the light wind conditions that adversely affect satellite altimeters and scatterometers, it seems likely that the small-scale waves intermittently vanish, leaving the intermediate and larger scale waves to determine the radar cross section.

Donelan and Pierson [16] pointed out that to generate short waves the wind must reach a threshold speed that is a function of the wavelength, surface tension, and viscosity. For the water temperature of the SOWEX dataset, their model (see [16, Figs. 4 and 6]) indicates that the threshold wind speed at 10-m height would be about 2 m/s to generate waves of 50-cm length, increasing to almost 6 m/s to generate waves of 1-cm length. Small-scale waves tend to be intermittent under light wind conditions because the wind speed can be highly variable (Fig. 7) and the waves decay rapidly when it drops below the required threshold. The intermediate-scale waves causing the distortions of Fig. 10 and the dominant waves such as the swell shown in Fig. 3 persist.

Kinsman [38] indicated that viscous damping causes waves of 1.7-cm wavelength, the boundary between gravity and capillary waves, to decay in about 4 s in the absence of forcing. The



Fig. 12. King Air west-to-east flight track at 160-m height over a bay in the northeast end of Big Kitoi Lake on Afognak Island in Alaska. The flight line is in the center of the figure, and the superimposed grid is in statute miles. The map was generated with National Geographic TOPO! software, and the elevations and depths are in feet.

viscous decay time would be about half an hour for waves of 0.5 m length, 2 h for 1-m waves, and 200 h for waves of 10-m length.

The viscous damping life spans and wave group velocities suggest the spatial scale on which the mss minimum might vary under light wind conditions. Waves of 10-m length could be generated by a 3- or 4-m/s wind over a 20–40-km fetch in about 4–8 h. Their wave energy would only propagate 3.5 km in an hour. The energy for waves of 1-m length would propagate about 2.2 km in their 2-h life. Waves of half-meter length could only affect a distance of 0.4 km during their half-hour life span. When you consider that this distance is represented by just over one-sixth of the 0.02° latitude divisions in Figs. 7 and 11 (slightly greater than the width of circles representing the SRA mss values), it becomes apparent that it is difficult for waves less than a meter in length to effect regions where they are not being generated.

The dominant waves generated by the wind in the open ocean could propagate for months if they did not encounter an opposing wind or a beach, but they quickly leave the generation area as the wind subsides. The dominant waves encountered in a region of light winds (Fig. 3) have generally arrived from another area and lost some of their original steepness.

A sinusoidal swell of 1.5-m crest-to-trough height (matching the 2.1 m H_S of Fig. 3) and 140-m wavelength (0.106-Hz wave frequency, an approximate centroid for the bimodal peak in Fig. 2) has a maximum slope of 1.9° and $mss = 0.0006$. The computed mss for the wave slope profile of Fig. 3 is 0.0004. This suggests that about two-thirds of the 0.0015 mss minimum observed by the SRA was contributed by the 1–10-m wavelength region. It is reasonable to expect that waves of 1–10-m length, such as caused the distortions in the images of Fig. 10, could account for the bulk of the minimum mss value in a

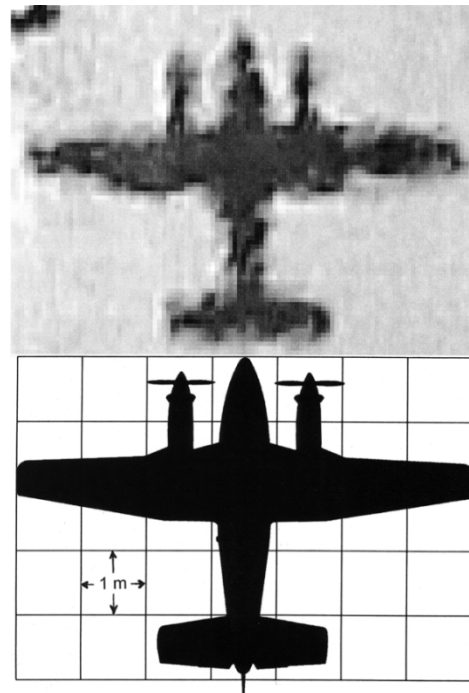


Fig. 13. Image of King Air seen in (top) down-looking video and (bottom) silhouette of aircraft with superimposed grid indicating the image size on the lake surface.

geographic area of light winds, smoothing over the temporal and spatial fluctuations in the local wind field.

VI. MSS NEAR LAND-WATER INTERFACE UNDER MODERATE WIND

On September 6, 2002, the National Oceanic and Atmospheric Administration (NOAA) Environmental Technology Laboratory was conducting surveys just north of Kodiak Island, AK, using the NOAA Fish Lidar [39], [40] on a Beech King Air aircraft. The thick line just below the center of Fig. 12 shows a short flight segment across a small bay (58.19°N , 152.38°W) of about 320-m east–west extent at the northeast end of Big Kitoi Lake on Afognak Island.

The wind at the 160-m aircraft height above the bay was 10 m/s from the west and the turbulence was great enough to make it unsafe to move around the aircraft to adjust the lidar. The air temperature reported at Kodiak and indicated by the Heitronics KT 15.85 D radiometer measurements made from the King Air aircraft over land was 13.5°C . The Heitronics radiometer measured the lake surface water temperature to be 14.5°C , although it indicated the water temperature in the bay was only 11.5°C .

Over open water the wind speed at 10-m height would be expected to be about 8 m/s and the mss about 0.03 [31]. But with the high relief of the heavily wooded adjacent terrain and the short over-water distance, the boundary layer profile would be changing spatially.

Fig. 13 shows the image of the King Air in the down-looking video as it neared the eastern shore of the bay and the aircraft silhouette. As in the top left panel of Fig. 9, the grid superimposed on the silhouette indicates the dimensions of the image

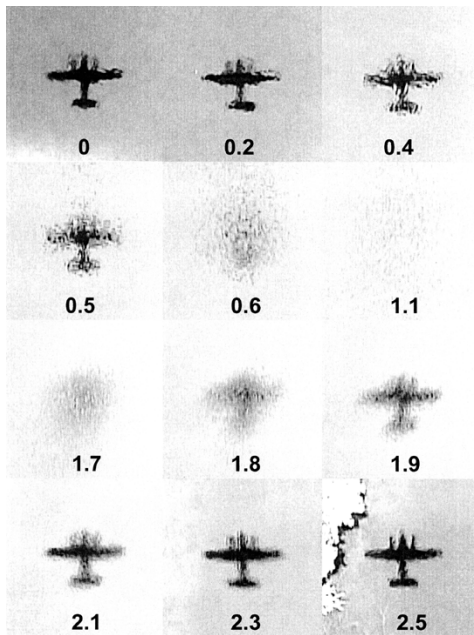


Fig. 14. Sequence of 12 down-looking video frames along the flight segment of Fig. 12, cropped to a width of 14 m on the surface, with incremental time in seconds indicated at the bottom of each frame.

on the lake surface, which are half the actual dimensions of the aircraft. The video image readily identifies the aircraft as a King Air and not a Fokker F-27.

The image in Fig. 13 is remarkably clear considering that the 160-m King Air height above the bay was five times higher than the Fokker F-27 height above the Southern Ocean. Since the King Air is about half the size of the Fokker, BW (Fig. 8) would have to be about one-tenth the values corresponding to the simulated images of Fig. 9 to produce the same effect. Equation (11) indicates that the small-scale mss values would have to be two orders of magnitude smaller than those shown in Fig. 9. The small-scale mss on the bay surface for the image of Fig. 13 was about 0.000 001. The aircraft was only a couple of meters from the shore, indicated by the dark area in the upper left-hand corner.

Fig. 14 shows a sequence of 12 video frames spanning 2.5 s. The zero time reference was shortly after the King Air left the west shore of the bay, and the sequence ends just before the frame shown in Fig. 13. The aircraft was flying east with a ground speed of 76 m/s, so the distance traversed in Fig. 14 was only 190 m, about the same as the distance traversed relative to the dominant waves for each 2-s SRA mss determination in the Southern Ocean.

The initial aircraft image (0 s) is crisp. About 30 m further from shore (0.4 s) it is principally distorted by waves of about a half-meter length propagating in the north-south direction. The small-scale roughness appears minimal and the half-meter waves were probably generated by the west wind in the main part of the lake and diffracted and refracted through the narrow bay inlet north of the flight line.

Big Kitoi Lake is shallow with a maximum depth of only 16 ft. Depth variation in the bay where the aircraft reflections were observed was not available. The presence of the half-meter waves suggests that the absence of small-scale waves was due

to either surfactants and/or low surface wind near the shoreline due to sheltering by the heavily wooded terrain.

Eight meters further (0.5 s), the south propagating waves no longer dominate and the effect of small-scale roughness is apparent. In another 8 m, the small-scale roughness dominates (0.6 s) and the aircraft image soon disappears entirely (1.1 s). The last six images in the Fig. 14 sequence (1.7–2.5 s) are similar to the sequence of simulated images shown in Fig. 9, with the mss decreasing by more than two orders of magnitude over a 60-m distance.

VII. SUMMARY AND CONCLUSION

The present study did not deal with fully developed conditions, but mainly with a light and variable wind in which the gravity-capillary waves exhibited large temporal and spatial variations. It did not attempt to quantify the spectrum, but simply to put an intuitive “face” on the sea surface under those highly volatile conditions.

It is convenient to think in terms of three wavelength scales on the sea surface: small-scale waves, 1–10-m intermediate waves, and large-scale waves. When the small-scale waves damped in the open ocean due to lack of wind or the presence of surfactants, the resulting water surface was smooth enough to reflect an image of an aircraft at a height of 30 m. The reflection still exhibited significant distortions due to the persistence of the intermediate-scale waves which, along with the dominant waves, maintained a minimum mss value of about 0.0015 for the Southern Ocean measurements of this study.

A simple optical model for the small-scale roughness of the water surface as producing an effect beamwidth which diffuses the aircraft image can be used to relate the appearance of the aircraft image in the video to the small-scale mean square slope.

The variation of backscattered power with incidence angle measured by a scanning radar altimeter operating at 36 GHz (Ka-band) provides a very sensitive determination of mss under light wind conditions which should be nearly equal to the optical value. The microwave estimate of mss correlated better with the optical assessment from the aircraft appearance in the down-looking video than it did with the wind speed at 30-m height, as would be expected since they were both direct measures of the surface. In the regions of lowest small-scale optical mss, the 0.0015 microwave minimum value was consistent with the estimate from the visual appearance of the average of the video images which were distorted by the intermediate and large-scale waves.

Despite a 10-m/s turbulent wind at the 160-m aircraft height over a lake in Alaska, the down-looking video image near shore indicated that the small-scale mss was only about 0.000 001. This very low value possibly resulted from a combination of sheltering by the heavily wooded terrain and the presence of surfactants. The absence of intermediate and large-scale waves resulted in an image within a few meters of the shoreline which almost exactly matched the aircraft silhouette.

These data suggest that an automated optical technique for assessing the small-scale mss under light wind conditions could be implemented with a nadir-looking digital camera and an algorithm that related the small-scale mss to the aircraft height

and the standard deviation of the image pixels or their frequency content. The aircraft height could be adjusted to optimize sensitivity, flying lower as the average mss increased.

This optical technique would not produce the same level of quantitative data as a laser slope meter, but it might provide low-cost information on mss with high temporal and spatial resolution for investigations that could not afford more sophisticated equipment. Digital video camera data could be sent to a computer over a firewire connection to provide real-time analysis. The technique might even work in a bistatic mode from fixed platforms using a dark target with a series of horizontal and vertical slots of different widths and spacings cut in it to allow the sky light through, after the manner of a traditional optical resolution chart.

ACKNOWLEDGMENT

The excellent technical support provided by D. E. Hines, C. Maher, and D. Parkin during SOWEX was greatly appreciated. The Alaskan video was provided by T. Veenstra (Airborne Technologies, Inc.), and the pilot was P. Johnson (Dynamic Aviation).

REFERENCES

- [1] G. T. Mitchum, D. W. Hancock, III, G. S. Hayne, and D. C. Vandemark, " σ^0 blooms in the TOPEX radar altimeter data," *J. Atmos. Oceanic Technol.*, vol. 21, pp. 1232–1245, Aug. 2004.
- [2] W. J. Plant, "Effects of wind variability on scatterometry at low wind speeds," *J. Geophys. Res.*, vol. 105, pp. 16 899–16 910, 2000.
- [3] K. Shankaranarayanan and M. A. Donelan, "A probabilistic approach to scatterometer model function verification," *J. Geophys. Res.*, vol. 106, pp. 19969–19990, 2001.
- [4] M. L. Banner, W. Chen, E. J. Walsh, J. Jensen, S. Lee, and C. B. Fandry, "The Southern Ocean Waves Experiment. Part I: Overview and mean results," *J. Phys. Oceanogr.*, vol. 29, pp. 2130–2145, 1999.
- [5] W. Chen, M. L. Banner, E. J. Walsh, J. Jensen, and S. Lee, "The Southern Ocean Waves Experiment, Part II. Sea-surface response to wind speed and wind stress variations," *J. Phys. Oceanogr.*, vol. 31, pp. 174–198, 2001.
- [6] E. J. Walsh, L. K. Shay, H. C. Graber, A. Guillaume, D. Vandemark, D. E. Hines, R. N. Swift, and J. F. Scott, "Observations of surface wave-current interaction during SWADE," *Global Atmos. Ocean Syst.*, vol. 5, pp. 99–124, 1996.
- [7] C. W. Wright, E. J. Walsh, D. Vandemark, W. B. Krabill, A. Garcia, S. H. Houston, M. D. Powell, P. G. Black, and F. D. Marks, "Hurricane directional wave spectrum spatial variation in the open ocean," *J. Phys. Oceanogr.*, vol. 31, pp. 2472–2488, 2001.
- [8] E. J. Walsh, C. W. Wright, D. Vandemark, W. B. Krabill, A. W. Garcia, S. H. Houston, S. T. Murillo, M. D. Powell, P. G. Black, and F. D. Marks, "Hurricane directional wave spectrum spatial variation at landfall," *J. Phys. Oceanogr.*, vol. 32, pp. 1667–1684, 2002.
- [9] M. A. Fischler and R. C. Bolles, "Random sample consensus—A paradigm for model-fitting with applications to image-analysis and automated cartography," *Commun. ACM*, vol. 24, no. 6, pp. 381–395, Jun. 1981.
- [10] D. E. Barrick, "Rough surface scattering based on the specular point theory," *IEEE Trans. Antennas Propagat.*, vol. AP-16, pp. 449–454, 1968.
- [11] G. R. Valenzuela, "Theories for the interaction of electromagnetic and oceanic waves—A review," *Bound. Layer Meteorol.*, vol. 13, pp. 61–85, 1978.
- [12] D. E. Barrick, "Wind dependence of quasispecular microwave sea scatter," *IEEE Trans. Antennas Propagat.*, vol. AP-22, pp. 135–136, 1974.
- [13] P. A. Hwang and O. H. Shemdin, "The dependence of sea surface slope on atmospheric stability and swell conditions," *J. Geophys. Res.*, vol. 93, pp. 13 903–13 912, 1988.
- [14] T. Hara, E. J. Bock, and D. Lyzenga, "In situ measurements of capillary—Gravity wave spectra using a scanning laser slope gauge and microwave radars," *J. Geophys. Res.*, vol. 99, pp. 12 593–12 602, 1994.
- [15] T. Hara, E. J. Bock, J. B. Edson, and W. R. McGillis, "Observation of short wind waves in coastal waters," *J. Phys. Oceanogr.*, vol. 28, pp. 1425–1438, 1998.
- [16] M. A. Donelan and W. J. Pierson, Jr., "Radar scattering and equilibrium ranges in wind-generated waves with application to scatterometry," *J. Geophys. Res.*, vol. 92, pp. 4971–5029, 1987.
- [17] J. R. Apel, "An improved model of the ocean surface wave vector spectrum and its effects on radar backscatter," *J. Geophys. Res.*, vol. 99, pp. 16 269–16 291, 1994.
- [18] R. Romeiser, W. Alpers, and V. Wismann, "An improved composite surface model for the radar backscattering cross section of the ocean surface. Part I: Theory of the model and optimization/validation by scatterometer data," *J. Geophys. Res.*, vol. 102, pp. 25 237–25 250, 1997.
- [19] T. Elfouhaily, B. Chapron, K. Katsaros, and D. Vandemark, "A unified directional spectrum for long and short wind-driven waves," *J. Geophys. Res.*, vol. 102, pp. 15 781–15 796, 1997.
- [20] Yu. G. Trokhimovski, "Gravity-capillary wave curvature spectrum and mean-square slope retrieved from microwave radiometric measurements (Coastal Ocean probing experiment)," *J. Atmos. Oceanic Tech.*, vol. 17, pp. 1259–1270, 2000.
- [21] G. S. Brown, "Quasispecular scattering from the air—sea interface," in *Surface Waves and Fluxes*. Boston, MA: Kluwer, 1990, vol. 2, Remote Sensing, ch. 10, pp. 1–39.
- [22] F. W. Millet and K. F. Warnick, "Validity of rough surface backscattering models," *Waves Random Media*, vol. 14, pp. 327–347, Jul. 2004.
- [23] F. C. Jackson, W. T. Walton, D. E. Hines, B. A. Walter, and C. Y. Peng, "Sea surface mean square slope from Ku-band backscatter data," *J. Geophys. Res.*, vol. 97, pp. 11 411–11 427, 1992.
- [24] A. G. Voronovich and V. U. Zavorotny, "Theoretical model for scattering of radar signals in Ku- and C-bands from a rough sea surface with breaking waves," *Waves Random Media*, vol. 11, pp. 247–269, 2001.
- [25] W. J. Plant, "A stochastic, multiscale model of microwave backscatter from the ocean," *J. Geophys. Res.*, vol. 107(C9), no. 3120, pp. 3-1–3-21, Sep. 2002. DOI:10.1029/2001JC000909.
- [26] M. A. Donelan, A. J. Hamilton, and W. H. Hui, "Directional spectra of wind-generated waves," *Philos. Trans. R. Soc. London, Ser. A*, vol. 315, pp. 509–562, 1985.
- [27] W. J. Plant, "A two-scale model of short wind generated waves and scatterometry," *J. Geophys. Res.*, vol. 91, pp. 10 735–10 749, 1986.
- [28] M. L. Banner, "Equilibrium spectra of wind waves," *J. Phys. Oceanogr.*, vol. 20, pp. 966–984, 1990.
- [29] B. Jahne and K. S. Riemer, "Two-dimensional wave number spectra of small-scale water surface waves," *J. Geophys. Res.*, vol. 95, pp. 11 531–11 546, 1990.
- [30] B. Chapron, V. Kerbaol, D. Vandemark, and T. Elfouhaily, "Importance of peakedness in sea surface slope measurements and applications," *J. Geophys. Res.*, vol. 105, pp. 17 195–17 202, 2000.
- [31] E. J. Walsh, D. C. Vandemark, C. A. Friehe, S. P. Burns, D. Khelif, R. N. Swift, and J. F. Scott, "Measuring sea surface mean square slope with a 36-GHz scanning radar altimeter," *J. Geophys. Res.*, vol. 103, pp. 12 587–12 601, 1998.
- [32] C. S. Cox and W. H. Munk, "Measurement of the roughness of the sea surface from photographs of the sun's glitter," *J. Opt. Soc. Amer.*, vol. 44, pp. 838–850, 1954.
- [33] ———, "Statistics of the sea surface derived from sun glitter," *J. Marine Res.*, vol. 13, pp. 198–227, 1954.
- [34] ———, "Slopes of the sea surface deduced from photographs of sun glitter," *Bull. Scripps Inst. Oceanogr.*, vol. 6, pp. 401–487, 1956.
- [35] J. A. Shaw and J. H. Churnside, "Scanning-laser glint measurements of sea-surface slope statistics," *Appl. Opt.*, vol. 36, no. 18, pp. 4202–4213, Jun. 20, 1997.
- [36] D. R. Thompson and R. F. Gasparovic, "Intensity modulation in SAR images of internal waves," *Nature*, vol. 320, pp. 345–348, 1986.
- [37] R. Romeiser, A. Schmidt, and W. Alpers, "A three-scale composite surface model for the ocean wave-radar modulation transfer function," *J. Geophys. Res.*, vol. 99, pp. 9785–9801, 1994.
- [38] B. Kinsman, *Wind Waves, Their Generation and Propagation on the Ocean Surface*. Englewood Cliffs, NJ: Prentice-Hall, 1965.
- [39] J. H. Churnside, J. J. Wilson, and V. V. Tatarskii, "Airborne lidar for fisheries applications," *Opt. Eng.*, vol. 40, pp. 406–414, 2001.
- [40] J. H. Churnside and J. J. Wilson, "Airborne lidar imaging of salmon," *Appl. Opt.*, vol. 43, pp. 1416–1424, 2004.



Edward J. Walsh (M'74–SM'03) received the B.S. and Ph.D. degrees in electrical engineering from Northeastern University, Boston, MA, in 1963 and 1967, respectively.

From 1967 to 1970, he served at the National Aeronautics and Space Administration (NASA) Electronics Research Center, Cambridge, MA, both as a civil servant and while on active duty in the U.S. Army as a Captain in the Signal Corps. Since 1970, he has been with what is now the NASA Wallops Flight Facility, Goddard Space Flight Center, involved in radar remote sensing of the sea. He is presently on assignment for NASA at the National Oceanic and Atmospheric Administration Environmental Technology Laboratory, Boulder, CO, and using a scanning radar altimeter to measure sea-surface roughness, directional wave spectra, and rain rate in hurricanes. He is an author on 57 peer-reviewed articles.

Dr. Walsh is the recipient of the 1975 NASA Outstanding Scientific Achievement Award and the 2001 NRL Alan Berman Research Publication Award. He is a member of Commission F of URSI.



Michael L. Banner has been involved for over 30 years in fundamental investigations of elusive air–sea interaction processes on the wind-driven sea surface, especially related to breaking waves. He has gathered and analyzed a variety of observational data from oil platforms and research aircraft, as well as in laboratory facilities. In parallel, he has carried out model studies on long-standing problems in nonlinear wave dynamics and air–sea interaction. His present research effort is focused on improving model forecasts of dangerous sea states and air–sea

interaction in severe marine weather conditions, when wave breaking is prevalent.



James H. Churnside received the Ph.D. degree from the Oregon Graduate Center, Beaverton, in 1978, working on optical propagation through refractive turbulence in the clear atmosphere.

He then became a Member of the Technical Staff of The Aerospace Corporation, Los Angeles, CA, working on atmospheric propagation and laser speckle statistics. In 1985, he joined the National Oceanic and Atmospheric Administration Environmental Technology Laboratory, Boulder, CO, where he has worked on optical propagation, infrared emission from the atmosphere, and airborne optical sensing of the ocean. He has published 66 articles in refereed journals and holds three patents.

Dr. Churnside is a Fellow of the OSA and a member of SPIE, AGU, and TOS.



Joseph A. Shaw (M'84–SM'04) was born in Bozeman, MT. He received the B.S. degree in electrical engineering from the University of Alaska, Fairbanks, the M.S. degree in electrical engineering from the University of Utah, Salt Lake City, and the M.S. and Ph.D. degrees in optical sciences from the University of Arizona, Tucson, in 1987, 1989, 1994, and 1996, respectively.

He was an Electro-optical Engineer at the National Oceanic and Atmospheric Administration (NOAA) Environmental Technology Laboratory, Boulder, CO, from 1989 to 2001, where he developed infrared spectroradiometers and laser sensors for studying the Earth's atmosphere and oceans. In 2001, he became Associate Professor of electrical and computer engineering at Montana State University, Bozeman. His current research is in polarimetric and radiometric imaging and laser remote sensing.

Dr. Shaw is a Fellow of the OSA and a member of SPIE. For his contributions to optical remote sensing science, engineering, and education, he received a Presidential Early Career Award for Scientists and Engineers, the international Vaisala Award from the World Meteorological Organization, a NOAA Bronze Medal Award, and a NOAA Outstanding Scientific Paper Award.

Douglas C. Vandemark (M'88) received the B.S. degree in physics from Hope College, Holland, MI, and the M.S. degree in electrical engineering from the University of Massachusetts, Amherst, in 1986 and 1988, respectively.

He worked for the University of Massachusetts Microwave Remote Sensing Laboratory from 1986 to 1988 and for McDonnell Douglas Corporation from 1988 to 1990. Since 1990, he has been with NASA's Goddard Space Flight Center, Greenbelt, MD, where he has been involved in active and passive microwave remote sensing of the atmosphere and ocean. Particular interests include measurement of sea-surface wave spectra and slope statistics, satellite scatterometry and altimetry, and methods for improved estimation of air–sea mass and momentum fluxes.

C. Wayne Wright attended the Delaware Technical and Community College, Wilmington, from 1972 to 1974. He received the B.S. degree (cum laude) in computer science from the University of Maryland Eastern Shore, Princess Anne, in 1985.

From 1974 to 1977, he was self-employed in the broadcast and electronic manufacturing industries. From 1977 to 1979, he worked for the Computer Science Corporation at the Wallops Flight Center. From 1979 to the present, he has been a Civil Servant at what is now the NASA Goddard Space Flight Center, Wallops Flight Facility, Wallops Island, VA. His research interests include design, development, and application of airborne remote sensing lidar and radar instruments. He is a Principal Investigator for the application of airborne metric and fluorescence lidar to coral reef mapping and monitoring and for the measurement of coral spawn for monitoring coral reefs. He is also a Co-Investigator for scanning radar altimeter measurements in hurricanes.

Jorgen B. Jensen, photograph and biography not available at the time of publication.



Sunhee Lee received the Ph.D. degree in geophysics from Australian National University, Canberra, in 1985.

From 1985 to 1987, she held the position of Lecturer of applied geology at the University of South Pacific, Suva, Fiji. During 1988–1989, she was a Research Fellow in the Department of Earth Sciences, Monash University, Victoria, Australia. Since 1989, she has been with the Australian Commonwealth Scientific and Industrial Research Organization, Atmospheric Research, first as Senior Project Scientist (1989–1998) and then as Principal Project Scientist, Air Pollutants: Sources, Modeling and Exposure Team (1998–present).